

DISTRIBUTED MODEL CONSTRUCTION IN RADIO INTERFEROMETRIC CALIBRATION

Sarod Yatawatta

ASTRON, The Netherlands Institute for Radio Astronomy,
The Netherlands.
Email: yatawatta@astron.nl

ABSTRACT

Calibration of a typical radio interferometric array yields thousands of parameters as solutions. These solutions contain valuable information about the systematic errors in the data (ionosphere and beam shape). This information could be reused in calibration to improve the accuracy and also can be fed into imaging to improve the fidelity. We propose a distributed optimization strategy to construct models for the systematic errors in the data using the calibration solutions. We formulate this as an elastic net regularized distributed optimization problem which we solve using the alternating direction method of multipliers (ADMM) algorithm. We give simulation results to show the feasibility of the proposed distributed model construction scheme.

Index Terms— Calibration, Radio interferometry, Array processing, Ionosphere, Beam model

1. INTRODUCTION

Radio interferometric observations are almost always affected by systematic errors. During calibration, these systematic errors are estimated along many directions in the sky using compact celestial sources as guide beacons. In addition, the corrupting signals are also subtracted from the data to reveal weaker signals of interest. Large volumes of data need to be calibrated to deliver the science goals of modern radio astronomy. As a secondary outcome of calibration, hundreds of thousands of parameters are obtained as calibration solutions and are stored as metadata.

The main sources of systematic errors in radio interferometric data are the ionosphere and the receiver beam shape. The effect of ionosphere is mostly represented as a phase (or total electron content) screen in radio astronomy [1, 2] as well as in other applications such as space weather [3]. The calibration solutions along the directions of compact sources are used to build phase screens [1, 2, 4] and this is further improved to operate in real time [5]. Faraday rotation of incoming radiation is an additional complication caused by the ionosphere (that can be seen with dual polarized antennae) and external information such as GNSS (global navigation satellite system) satellites are used to model this [6, 7, 8]. It is noteworthy that phase screen models have limited accuracy for science goals that demand high dynamic ranges [9].

The receiver beam shape has traditionally been estimated using holographic techniques [10, 11, 12]. Recent surge in the use of unmanned aerial vehicles (drones) have enabled their use in beam shape estimation as well [13, 14]. It is also possible to use calibration solutions to obtain beam models [15]. Once accurate models for the

ionosphere and the beam shape have been obtained, image fidelity can be improved by incorporating such models into the imaging process [16, 17].

In this paper, we propose a method to construct a unified model for the ionosphere and the beam shape. The novelty (relation to prior work) is as follows: (i) We extend the scalar models (single polarization) [1, 2, 5, 15] to handle data taken with dual polarized receivers. Our model incorporates the refraction and the Faraday rotation due to the ionosphere into one. (ii) We create a unified model for both the ionosphere and the beam shape and can be directly used by imaging algorithms [16, 17]. We enforce elastic net regularization [18] during model creation. The power constraint comes naturally because the received signals have finite power [15]. The sparseness is more subtle, but arises because the relative difference in the ionosphere seen by receivers close together on Earth is small [19, 20, 21]. Therefore, sparseness minimizes overfitting, for example when there is no differential Faraday rotation between stations. (iii) We propose a distributed optimization scheme using the alternating direction method of multipliers (ADMM) [22]. This scheme matches nicely with the distributed calibration schemes in use [23, 24], and also makes our algorithm computationally efficient.

The rest of the paper is organized as follows: We give a brief introduction to radio interferometric calibration and models for systematic errors in section 2. We propose a distributed model construction method based on consensus optimization in section 3. We show the feasibility of the proposed method in section 4 using simulated data before drawing our conclusions in section 5. Notation: Matrices and vectors are denoted by bold upper and lower case letters as \mathbf{J} and \mathbf{v} , respectively. The transpose and the Hermitian transpose are given by $(\cdot)^T$ and $(\cdot)^H$, respectively. The matrix Frobenius norm is given by $\|\cdot\|$ and the l_1 norm by $\|\cdot\|_1$. The set of real and complex numbers are denoted by \mathbb{R} and \mathbb{C} , respectively. The identity matrix (size $N \times N$) is given by \mathbf{I}_N .

2. RADIO INTERFEROMETRIC DATA MODEL

We consider an array with N stations and the observed data $\mathbf{V}_{pqf} \in \mathbb{C}^{2 \times 2}$ at the baseline formed by stations p and q at frequency f is given by [25]

$$\mathbf{V}_{pqf} = \sum_{k=1}^K \mathbf{J}_{pkf} \mathbf{C}_{pqkf} \mathbf{J}_{qkf}^H + \mathbf{N}. \quad (1)$$

The data consists of the known signals from K sources in the sky $\mathbf{C}_{pqkf} \in \mathbb{C}^{2 \times 2}$, $p, q \in [1, N]$, $k \in [1, K]$ corrupted by the systematic errors $\mathbf{J}_{pkf}, \mathbf{J}_{qkf} \in \mathbb{C}^{2 \times 2}$. The systematic errors represent the cumulative effect of the ionosphere and the beam shape and also the receiver electronics. We consider the data (taken at F distinct

This work was supported by Netherlands eScience Center (project DIRAC, grant 27016G05).

frequencies) to be stored across a network of computers. Using distributed calibration [23], we estimate the systematic errors \mathbf{J}_{pkf} for all p, k and f and we also store the solutions across the network of computers.

Provided that the K directions are spread across the full field of view, our objective is to create a model for the systematic errors across the field of view of each station. We use G basis functions to cover the field of view and these basis functions represent the variation of the systematic errors both spatially as well as with frequency. Given that there are $F \times K$ solutions per each station, we assume $G \ll F \times K$. Let the k -th direction have spatial coordinates (α_k, β_k) , and at frequency f , let the i -th basis function be $\phi_i(\alpha_k, \beta_k, f)$, $i \in [1, G]$.

Based on the model $\mathbf{X} \in \mathbb{C}^{2N \times 2G}$ and the basis functions evaluated along the k -th direction at frequency f , $\Phi_{\alpha_k \beta_k f} \in \mathbb{C}^{2G \times 2}$, we can represent systematic errors for all N stations along the k -th direction $\mathbf{J}_{kf} \in \mathbb{C}^{2N \times 2}$ as

$$\mathbf{J}_{kf} = \mathbf{X} \Phi_{\alpha_k \beta_k f} \quad (2)$$

where

$$\mathbf{X} \triangleq \begin{bmatrix} \mathbf{X}_{11} & \mathbf{X}_{12} & \dots & \mathbf{X}_{1G} \\ \mathbf{X}_{21} & \mathbf{X}_{22} & \dots & \mathbf{X}_{2G} \\ \dots & \dots & \dots & \dots \\ \mathbf{X}_{N1} & \mathbf{X}_{N2} & \dots & \mathbf{X}_{NG} \end{bmatrix}, \quad (3)$$

$$\Phi_{\alpha_k \beta_k f} \triangleq \begin{bmatrix} \phi_1(\alpha_k, \beta_k, f) \\ \phi_2(\alpha_k, \beta_k, f) \\ \dots \\ \phi_G(\alpha_k, \beta_k, f) \end{bmatrix} \otimes \mathbf{I}_2, \quad \mathbf{J}_{kf} \triangleq \begin{bmatrix} \mathbf{J}_{1kf} \\ \mathbf{J}_{2kf} \\ \dots \\ \mathbf{J}_{Nkf} \end{bmatrix}.$$

Each $\mathbf{X}_{pi} \in \mathbb{C}^{2 \times 2}$, $p \in [1, N]$, $i \in [1, G]$ in \mathbf{X} represents the contribution of the i -th basis function towards the model of the systematic errors of the p -th station. Note that each \mathbf{X}_{pi} is independent of spatial coordinates or frequency.

It seems straightforward to estimate \mathbf{X} by augmenting many calibration solutions \mathbf{J}_{kf} and inverting (2). However, the solutions attainable for (1) are $\mathbf{J}_{kf} \mathbf{U}_{kf}$ where $\mathbf{U}_{kf} \in \mathbb{C}^{2 \times 2}$ is an unknown unitary matrix $\mathbf{U}_{kf} \mathbf{U}_{kf}^H = \mathbf{I}$. The reason for this unitary ambiguity is that \mathbf{C}_{pqkf} in (1) is scalar diagonal for most celestial sources ($= \gamma \mathbf{I}_2$, $\gamma \in \mathbb{C}$). Notably, the unitary ambiguity will be different for each direction k and for each frequency f . Therefore, we cannot use (2) directly to find \mathbf{X} .

3. DISTRIBUTED MODEL CONSTRUCTION

In order to overcome the inherent unitary ambiguity, we reformulate our problem as follows. Taking the product

$$\mathbf{J}_{pkf} \mathbf{C}_{pqkf} \mathbf{J}_{qkf}^H = \mathbf{A}_p \mathbf{X} \Phi_{\alpha_k \beta_k f} \tilde{\mathbf{C}}_{pqkf} (\mathbf{A}_q \mathbf{X} \Phi_{\alpha_k \beta_k f})^H \quad (4)$$

using calibration solutions \mathbf{J}_{pkf} and \mathbf{J}_{qkf} , we see that the unitary ambiguity cancels out because it is the same for both \mathbf{J}_{pkf} and \mathbf{J}_{qkf} and because \mathbf{C}_{pqkf} is diagonal. In (4), $\mathbf{A}_p \in \mathbb{R}^{2 \times 2N}$ is a matrix of zeros except at the p -th 2×2 block it is \mathbf{I}_2 ,

$$\mathbf{A}_p \triangleq [\mathbf{0} \ \mathbf{0} \ \dots \ \mathbf{I}_2 \ \dots \ \mathbf{0}] \quad (5)$$

(and \mathbf{A}_q likewise). The model for the p -th station is given by $\mathbf{A}_p \mathbf{X}$. The (updated) sky contribution $\tilde{\mathbf{C}}_{pqkf}$ used in constructing the model need not be equal to \mathbf{C}_{pqkf} which is used in calibration. Both

$\tilde{\mathbf{C}}_{pqkf}$ and \mathbf{C}_{pqkf} are almost always diagonal matrices (because the sky signal is intrinsically unpolarized). We define a cost function as

$$h(\mathbf{X}) \triangleq \sum_{pqkf} \|\mathbf{J}_{pkf} \mathbf{C}_{pqkf} \mathbf{J}_{qkf}^H - \mathbf{A}_p \mathbf{X} \Phi_{\alpha_k \beta_k f} \tilde{\mathbf{C}}_{pqkf} (\mathbf{A}_q \mathbf{X} \Phi_{\alpha_k \beta_k f})^H\|^2 \quad (6)$$

where the inclusion of $\tilde{\mathbf{C}}_{pqkf}$ and \mathbf{C}_{pqkf} in the cost function acts as a weighting, i.e., giving larger weights to solutions along the directions with large intensities, and therefore with higher signal to noise ratios. Also different k -s will have different fluxes, not all normalized in the input model, so this also acts as a normalization across all directions in the sky.

Let the data be partitioned into different frequency subsets and let the j -th partition contain frequencies given by the set \mathcal{F}_j . Each \mathcal{F}_j is assumed to represent the data stored in one compute node. We separate the summation in (6) as

$$h(\mathbf{X}) = \sum_j h_j(\mathbf{X}) \quad (7)$$

where

$$h_j(\mathbf{X}) = \sum_{f \in \mathcal{F}_j} \sum_{pqk} \|\mathbf{J}_{pkf} \mathbf{C}_{pqkf} \mathbf{J}_{qkf}^H - \mathbf{A}_p \mathbf{X} \Phi_{\alpha_k \beta_k f} \tilde{\mathbf{C}}_{pqkf} (\mathbf{A}_q \mathbf{X} \Phi_{\alpha_k \beta_k f})^H\|^2 \quad (8)$$

correspond to the cost function local to the j -th compute node (\sum_j implies summing over all compute nodes' cost functions).

The model is constructed by minimizing (6) or (7) with elastic net regularization [18]

$$\mathbf{X} = \arg \min_{\mathbf{X}} \sum_j h_j(\mathbf{X}) + \lambda \|\mathbf{X}\|^2 + \mu \|\mathbf{X}\|_1 \quad (9)$$

where $\lambda, \mu \in \mathbb{R}^+$. Solving (9) directly is not tractable and noting that each $h_j(\mathbf{X})$ is calculated on different compute nodes, we redefine (9) as a consensus problem [22]

$$\mathbf{X}_1, \mathbf{X}_2, \dots, \mathbf{Z} = \arg \min_{\mathbf{X}_1, \mathbf{X}_2, \dots, \mathbf{Z}} \sum_j h_j(\mathbf{X}_j) + \lambda \|\mathbf{Z}\|^2 + \mu \|\mathbf{Z}\|_1 \quad (10)$$

subject to $\mathbf{X}_j = \mathbf{Z} \ \forall j$, and $\mathbf{X}_1, \mathbf{X}_2, \dots, \mathbf{Z} \in \mathbb{C}^{2N \times 2G}$.

The augmented Lagrangian for solving (10) using ADMM is

$$L(\mathbf{X}_1, \mathbf{X}_2, \dots, \mathbf{Z}, \mathbf{Y}_1, \mathbf{Y}_2, \dots) \quad (11)$$

$$= \sum_j h_j(\mathbf{X}_j) + \|\mathbf{Y}_j^H (\mathbf{X}_j - \mathbf{Z})\| + \frac{\rho}{2} \|\mathbf{X}_j - \mathbf{Z}\|^2$$

$$+ \lambda \|\mathbf{Z}\|^2 + \mu \|\mathbf{Z}\|_1$$

where $\rho \in \mathbb{R}^+$ is the penalty parameter and $\mathbf{Y}_j \in \mathbb{C}^{2N \times 2G}$ is the Lagrange multiplier local to compute node j .

The ADMM iterations for solving (10) are (using $n = 1, 2, \dots$ superscript for iteration number)

$$\mathbf{X}_j^{n+1} = \arg \min_{\mathbf{X}_j} L(\mathbf{X}_j, \mathbf{Z}^n, \mathbf{Y}_j^n) \quad (12)$$

$$\mathbf{Z}^{n+1} = \arg \min_{\mathbf{Z}} L(\mathbf{X}_1^{n+1}, \mathbf{X}_2^{n+1}, \dots, \mathbf{Z}, \mathbf{Y}_1^n, \mathbf{Y}_2^n, \dots) \quad (13)$$

$$\mathbf{Y}_j^{n+1} = \mathbf{Y}_j^n + \rho(\mathbf{X}_j^{n+1} - \mathbf{Z}^{n+1}). \quad (14)$$

Steps (12) and (14) are performed in a distributed manner at each compute node and the intermediate step (13) is performed at the fusion center. There is no closed form solution for (12) and we use the Riemannian trust region method [26, 27] to find a solution. The required gradient and Hessian operators are given in the appendix.

A solution for (13) is obtained in closed form as

$$\mathbf{Z} = \Psi_{\frac{2\mu}{2\lambda + \sum_{j'} \rho}} \left(\frac{1}{2\lambda + \sum_{j'} \rho} \sum_j (\mathbf{Y}_j + \rho \mathbf{X}_j) \right) \quad (15)$$

where $\Psi(\cdot)$ is the (matrix) soft threshold operator, its scalar version being $\Psi_\lambda(x) = \text{sign}(x)\max(|x| - \lambda, 0)$.

4. SIMULATIONS

We simulate an array with $N = 16$ stations, collecting data at $F = 10$ frequencies in the range [60, 180] MHz. Note that F can be many hundreds in real observations. The sky consists of $K = 60$ sources, spread across a field of view of 10 degrees in diameter. The beam shapes of each N stations are randomly generated Gaussians, with random pointing centers and footprints. The width of the beams are varied according to $1/f^2$. The source intensities are attenuated according to the average beam shape. As seen in Fig. 1, the sources at the center have higher intensities than at the edge of the field of view. To simulate the effect of the ionosphere, each beam shape

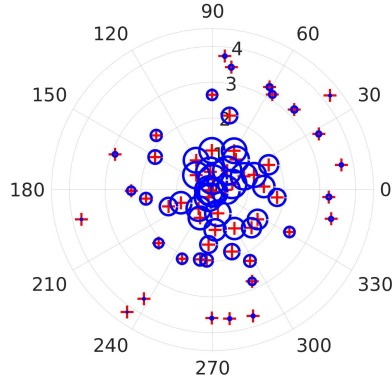


Fig. 1. Sky model spread across a field of view of 10 degrees in diameter. The blue circles are scaled according to the intensity of each source.

is multiplied by a complex number $\exp j(a_1\alpha/f + a_2\beta/f)$ where (α, β) are spatial coordinates and a_1, a_2 are drawn from $\mathcal{U}(-5, 5)$. Finally, each scalar beam shape is multiplied by a randomly generated rotation matrix $\in \mathbb{C}^{2 \times 2}$ to simulate the effect of Faraday rotation (rotation angle scales as $1/f^2$). Using this compound model, we calculate the calibration solutions \mathbf{J}_{kf} and multiply them with a random unitary matrix $\in \mathbb{C}^{2 \times 2}$. We also add noise (a random matrix $\in \mathbb{C}^{2N \times 2}$) to \mathbf{J}_{kf} with a norm that is 5% of $\|\mathbf{J}_{kf}\|$.

The basis functions $\Phi_{\alpha_k\beta_kf}$ in (3) are constructed by using 16 spherical harmonics (for spatial dependence) multiplied with 5 Bernstein bases (for frequency dependence). Therefore, $G = 16 \times 5 = 80 \ll F \times K = 10 \times 60 = 600$. We use 50 ADMM iterations, with penalty $\rho = 10$ and regularization parameters $\lambda = 40$ and $\mu = 10$. We show the primal ($\|\mathbf{X}_j^n - \mathbf{Z}^n\|$) and dual ($\|\mathbf{Z}^n - \mathbf{Z}^{n-1}\|$) residuals in Fig. 2. We see that the primal residual is much higher, mainly

because of the frequency dependence (Bernstein bases) not being representative enough.

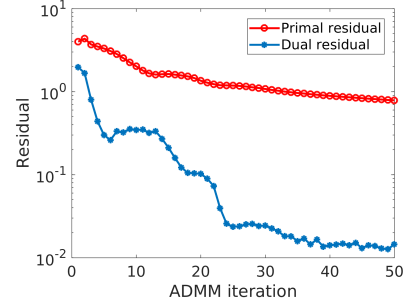


Fig. 2. Variation of primal and dual residuals with ADMM iteration.

We compare the solution obtained by (10) with the linear estimate obtained by solving (2). Note that the linear estimate is always inferior to the solution obtained by (10) because of the unitary ambiguities. We show the systematic error models constructed for one station in Figs. 3 and 4, showing the real and imaginary parts of the systematic errors for one correlation (XX). As expected, the consensus optimization based solution (with and without regularization) gives better results than the linear estimate.

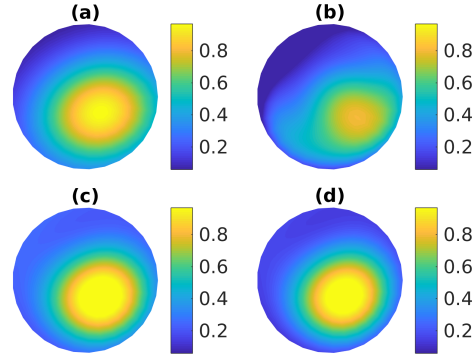


Fig. 3. XX systematic error real part across the full field of view: (a) ground truth (b) linear estimate (c) consensus without regularization (d) consensus with regularization.

In order to study the effect of elastic net regularization, we calculate the ground truth value of systematic errors \mathbf{J}_{kf} and the estimated systematic errors based on the constructed model $\hat{\mathbf{J}}_{kf}$ and find the difference (subject to a unitary ambiguity \mathbf{U} [28]) as $\|\mathbf{J}_{kf} - \hat{\mathbf{J}}_{kf}\mathbf{U}\|$. We call this *model construction error*. We evaluate the model construction error on a spatial grid of 30×30 directions (covering the full field of view) and average this over all N stations. The model construction error surface over the full field of view at $f = 100$ MHz is shown in Fig. 5. For comparison, we have also shown the average $\|\mathbf{J}_{kf}\|$ in Fig. 5 (a). We see the improvement due to elastic net regularization by comparing Fig. 5 (c) (no regularization) with Fig. 5 (d). The number of nonzero elements in the model \mathbf{X} in the case of Fig. 5 (c) is $2N \times 2G = 5120$ while with elastic net regularization, this value becomes 4131.

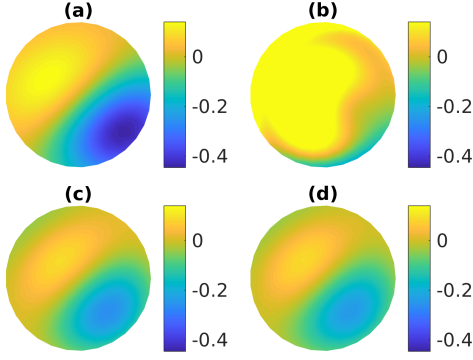


Fig. 4. XX systematic error imaginary part across the full field of view: (a) ground truth (b) linear estimate (c) consensus without regularization (d) consensus with regularization.

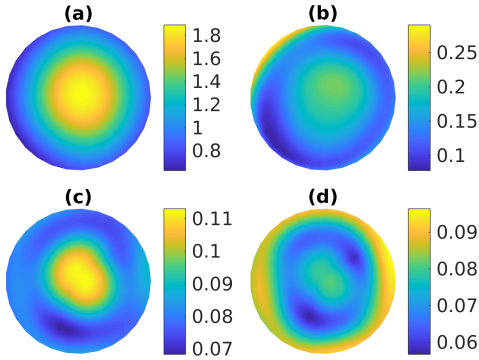


Fig. 5. Average model construction error across the full field of view: (a) norm of \mathbf{J}_{kf} (b) linear estimate (c) consensus without regularization (d) consensus with regularization.

The variation of the average model construction error (over the full field of view) with frequency is shown in Fig. 6. We can clearly see the improvement due to consensus optimization and elastic net regularization in Fig. 6.

5. CONCLUSIONS

We have formulated the construction of models for systematic errors in radio interferometric data as a distributed optimization problem. We solve this problem with the use of the ADMM algorithm and with elastic net regularization. Simulations show the feasibility of the proposed algorithm as well as the improvement gained by the elastic net regularization. Future work will focus on the application of this method to real observations and developing distributed software that increases computational speed.

APPENDIX: GRADIENT AND HESSIAN

The form of the original cost function (6) is structurally similar to the one considered in [23]. Therefore, by simple substitutions, it is

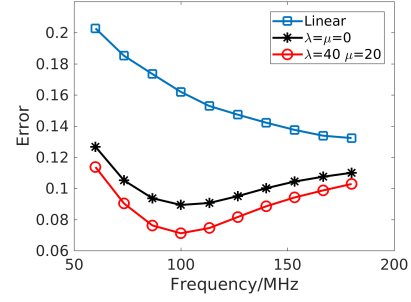


Fig. 6. Average model construction error variation with frequency.

possible to derive the gradient and the Hessian. We get the gradient of the augmented Lagrangian as

$$\text{grad}(L, \mathbf{X}_j) = \text{grad}(h_j(\mathbf{X}_j), \mathbf{X}_j) + \frac{1}{2} \mathbf{Y}_j + \frac{\rho}{2} (\mathbf{X}_j - \mathbf{Z}) \quad (16)$$

where

$$\begin{aligned} \text{grad}(h_j(\mathbf{X}), \mathbf{X}) &= - \sum_{f \in \mathcal{F}_j} \sum_{pqk} \left(\mathbf{A}_p^T \left(\mathbf{J}_{pkf} \mathbf{C}_{pqkf} \mathbf{J}_{qkf}^H \right. \right. \\ &\quad - \mathbf{A}_p \mathbf{X} \Phi_{\alpha\beta f} \tilde{\mathbf{C}}_{pqkf} \Phi_{\alpha\beta f}^H \mathbf{X}^H \mathbf{A}_q^T \Big) \mathbf{A}_q \mathbf{X} \Phi_{\alpha\beta f} \tilde{\mathbf{C}}_{pqkf}^H \Phi_{\alpha\beta f}^H \\ &\quad + \mathbf{A}_q^T \left(\mathbf{J}_{pkf} \mathbf{C}_{pqkf} \mathbf{J}_{qkf}^H \right. \\ &\quad \left. \left. - \mathbf{A}_p \mathbf{X} \Phi_{\alpha\beta f} \tilde{\mathbf{C}}_{pqkf} \Phi_{\alpha\beta f}^H \mathbf{X}^H \mathbf{A}_q^T \right)^H \mathbf{A}_p \mathbf{X} \Phi_{\alpha\beta f} \tilde{\mathbf{C}}_{pqkf} \Phi_{\alpha\beta f}^H \right). \end{aligned} \quad (17)$$

Similarly, the Hessian becomes

$$\text{Hess}(L, \mathbf{X}_j, \boldsymbol{\eta}) = \text{Hess}(h_j(\mathbf{X}_j), \mathbf{X}_j, \boldsymbol{\eta}) + \frac{\rho}{2} \boldsymbol{\eta} \quad (18)$$

where

$$\begin{aligned} \text{Hess}(h_j(\mathbf{X}), \mathbf{X}, \boldsymbol{\eta}) &= \sum_{f \in \mathcal{F}_j} \sum_{pqk} \left(\mathbf{A}_p^T \left(\mathbf{J}_{pkf} \mathbf{C}_{pqkf} \mathbf{J}_{qkf}^H \right. \right. \\ &\quad - \mathbf{A}_p \mathbf{X} \Phi_{\alpha\beta f} \tilde{\mathbf{C}}_{pqkf} \Phi_{\alpha\beta f}^H \mathbf{X}^H \mathbf{A}_q^T \Big) \mathbf{A}_q \boldsymbol{\eta} \\ &\quad - \mathbf{A}_p \left(\mathbf{X} \Phi_{\alpha\beta f} \tilde{\mathbf{C}}_{pqkf} \Phi_{\alpha\beta f}^H \boldsymbol{\eta}^H \right. \\ &\quad \left. + \boldsymbol{\eta} \Phi_{\alpha\beta f} \tilde{\mathbf{C}}_{pqkf} \Phi_{\alpha\beta f}^H \mathbf{X}^H \right) \mathbf{A}_q^T \mathbf{A}_q \mathbf{X} \Big) \Phi_{\alpha\beta f} \tilde{\mathbf{C}}_{pqkf}^H \Phi_{\alpha\beta f}^H \\ &\quad + \mathbf{A}_q^T \left(\mathbf{J}_{pkf} \mathbf{C}_{pqkf} \mathbf{J}_{qkf}^H \right. \\ &\quad - \mathbf{A}_p \mathbf{X} \Phi_{\alpha\beta f} \tilde{\mathbf{C}}_{pqkf} \Phi_{\alpha\beta f}^H \mathbf{X}^H \mathbf{A}_q^T \Big)^H \mathbf{A}_p \boldsymbol{\eta} \\ &\quad - \mathbf{A}_q \left(\mathbf{X} \Phi_{\alpha\beta f} \tilde{\mathbf{C}}_{pqkf} \Phi_{\alpha\beta f}^H \boldsymbol{\eta}^H \right. \\ &\quad \left. + \boldsymbol{\eta} \Phi_{\alpha\beta f} \tilde{\mathbf{C}}_{pqkf} \Phi_{\alpha\beta f}^H \mathbf{X}^H \right)^H \mathbf{A}_p^T \mathbf{A}_p \mathbf{X} \Big) \Phi_{\alpha\beta f} \tilde{\mathbf{C}}_{pqkf} \Phi_{\alpha\beta f}^H \end{aligned} \quad (19)$$

The only difference is in the gradient with respect to \mathbf{Z} , which is

$$\text{grad}(L, \mathbf{Z}) = \sum_j \frac{1}{2} (-\mathbf{Y}_j + \rho(-\mathbf{X}_j + \mathbf{Z})) + \lambda \mathbf{Z} + \mu \partial \|\mathbf{Z}\|_1 \quad (20)$$

where $\partial \|\mathbf{Z}\|_1$ is the subgradient of $\|\mathbf{Z}\|_1$.

6. REFERENCES

- [1] W.D. Cotton, "Ionospheric effects and imaging and calibration of VLA data," *Very Large Array (VLA) Scientific Memorandum 118*, pp. 1–12, 2007.
- [2] H. T. Intema, S. van der Tol, W. D. Cotton, A. S. Cohen, I. M. van Bommel, and H. J. A. Röttgering, "Ionospheric calibration of low frequency radio interferometric observations using the peeling scheme. I. Method description and first results," *Astronomy and Astrophysics*, vol. 501, pp. 1185–1205, July 2009.
- [3] J. Lee, Y. T. J. Morton, J. Lee, H. S. Moon, and J. Seo, "Monitoring and mitigation of ionospheric anomalies for GNSS-based safety critical systems: A review of up-to-date signal processing techniques," *IEEE Signal Processing Magazine*, vol. 34, no. 5, pp. 96–110, Sept 2017.
- [4] M. Mevius, S. v. d. Tol, V. N. Pandey, H. K. Vedantham, et al., "Probing ionospheric structures using the LOFAR radio telescope," *Radio Science*, vol. 51, no. 7, pp. 927–941, July 2016.
- [5] D. A. Mitchell, L. J. Greenhill, R. B. Wayth, R. J. Sault, C. J. Lonsdale, R. J. Cappallo, M. F. Morales, and S. M. Ord, "Real-time calibration of the Murchison widefield array," *IEEE Journal of Selected Topics in Signal Processing*, vol. 2, no. 5, pp. 707–717, Oct 2008.
- [6] Sotomayor-Beltran, C., Sobey, C., Hessels, J. W. T., de Bruyn, G., et al., "Calibrating high-precision Faraday rotation measurements for LOFAR and the next generation of low-frequency radio telescopes," *Astronomy and Astrophysics*, vol. 552, pp. A58, 2013.
- [7] B. S. Arora, J. Morgan, S. M. Ord, S. J. Tingay, et al., "Ionospheric modelling using GPS to calibrate the MWA. I: Comparison of first order ionospheric effects between GPS models and MWA observations," *Publications of the Astronomical Society of Australia*, vol. 32, 2015.
- [8] B. S. Arora, J. Morgan, S. M. Ord, S. J. Tingay, et al., "Ionospheric Modelling using GPS to Calibrate the MWA. II: Regional Ionospheric Modelling using GPS and GLONASS to Estimate Ionospheric Gradients," *Publications of the Astronomical Society of Australia*, vol. 33, pp. e031, July 2016.
- [9] P. L. Martin, J. D. Bray, and A. M. M. Scaife, "Limits on the validity of the thin-layer model of the ionosphere for radio interferometric calibration," *Monthly Notices of the Royal Astronomical Society*, vol. 459, pp. 3525–3531, July 2016.
- [10] P.F. Scott and M. Ryle, "A rapid method for measuring the figure of a radio telescope reflector," *Monthly Notices of the Royal Astronomical Society*, vol. 178, pp. 539–545, Aug. 1976.
- [11] J.C. Bennet, A.P. Anderson, P.A. McInnes, and J.T. Whitaker, "Microwave holographic metrology of large reflector antennas," *IEEE Trans. on Antennas and Propagation*, vol. AP-24, no. 3, pp. 295–303, May 1976.
- [12] G. R. Harp, R. F. Ackermann, Z. J. Nadler, et al., "Primary beam and dish surface characterization at the Allen telescope array by radio holography," *IEEE Transactions on Antennas and Propagation*, vol. 59, no. 6, pp. 2004–2021, June 2011.
- [13] C. Chang, C. Monstein, A. Refregier, A. Amara, A. Glauser, and S. Casura, "Beam Calibration of Radio Telescopes with Drones," *Publications of the Astronomical Society of Pacific*, vol. 127, pp. 1131, Nov. 2015.
- [14] D. C. Jacobs, J. Burba, L. Turner, and B. Stinnett, "An external calibrator for hydrogen observatories," in *2016 IEEE Conference on Antenna Measurements Applications (CAMA)*, Oct 2016, pp. 1–3.
- [15] S. Yatawatta, "Estimation of radio interferometer beam shapes using Riemannian optimization," *Experimental Astronomy*, vol. 35, pp. 469–487, Apr. 2013.
- [16] S. Bhatnagar, U. Rau, and K. Golap, "Wide-field wide-band Interferometric Imaging: The WB A-Projection and Hybrid Algorithms," *Astrophysical Journal*, vol. 770, pp. 91, June 2013.
- [17] C. Tasse, S. van der Tol, J. van Zwieten, G. van Diepen, and S. Bhatnagar, "Applying full polarization A-Projection to very wide field of view instruments: An imager for LOFAR," *Astronomy and Astrophysics*, vol. 553, pp. A105, May 2013.
- [18] Hui Zou and Trevor Hastie, "Regularization and variable selection via the elastic net," *Journal of the Royal Statistical Society: Series B (Statistical Methodology)*, vol. 67, no. 2, pp. 301–320, 2005.
- [19] C. J. Lonsdale, "Configuration Considerations for Low Frequency Arrays," in *From Clark Lake to the Long Wavelength Array: Bill Erickson's Radio Science*, N. Kassim, M. Perez, W. Junor, and P. Henning, Eds., Dec. 2005, vol. 345 of *Astronomical Society of the Pacific Conference Series*, p. 399.
- [20] S. van der Tol and A. J. van der Veen, "Ionospheric calibration for the LOFAR radio telescope," in *2007 International Symposium on Signals, Circuits and Systems*, July 2007, vol. 2, pp. 1–4.
- [21] S. J. Wijnholds, "Constraining ionospheric models with radio interferometric self calibration data," in *General Assembly and Scientific Symposium (URSI GASS), 2017 XXXVIIth URSI*, Aug 2017, pp. 1–4.
- [22] Stephen Boyd, Neal Parikh, Eric Chu, Borja Peleato, and Jonathan Eckstein, "Distributed optimization and statistical learning via the alternating direction method of multipliers," *Foundations and Trends® in Machine Learning*, vol. 3, no. 1, pp. 1–122, 2011.
- [23] S. Yatawatta, "Distributed radio interferometric calibration," *Monthly Notices of the Royal Astronomical Society*, vol. 449, no. 4, pp. 4506–4514, 2015.
- [24] M. Brossard, M. N. El Korso, M. Pesavento, R. Boyer, P. Larzabal, and S. J. Wijnholds, "Parallel Calibration for Sensor Array Radio Interferometers," *ArXiv e-prints*, Sept. 2016.
- [25] J. P. Hamaker, J. D. Bregman, and R. J. Sault, "Understanding radio polarimetry, paper I," *Astronomy and Astrophysics Supp.*, vol. 117, no. 137, pp. 96–109, 1996.
- [26] P.-A. Absil, C. G. Baker, and K. A. Gallivan, "Trust-region methods on Riemannian manifolds," *Found. Comput. Math.*, vol. 7, no. 3, pp. 303–330, July 2007.
- [27] N. Boumal, B. Mishra, P.-A. Absil, and R. Sepulchre, "Manopt, a Matlab toolbox for optimization on manifolds," *Journal of Machine Learning Research*, vol. 15, pp. 1455–1459, 2014.
- [28] S. Yatawatta, "On the interpolation of calibration solutions obtained in radio interferometry," *Monthly Notices of the Royal Astronomical Society*, vol. 428, no. 1, pp. 828–833, Jan. 2013.